

# Wavelet-Space Super-Resolution for Real-Time Rendering

Prateek Poudel<sup>1\*†</sup>, Prashant Aryal<sup>1†</sup>, Kirtan Kunwar<sup>1†</sup>, Navin Nepal<sup>1†</sup>,  
Dinesh Bania Kshatri<sup>1</sup>

<sup>1\*</sup>Department of Electronics and Computer Engineering, Thapathali Campus, IOE,  
Tribhuvan University, Kathmandu Nepal.

\*Corresponding author(s). E-mail(s): [prateekpoudel61@gmail.com](mailto:prateekpoudel61@gmail.com);

Contributing authors: [prashantaryal07@gmail.com](mailto:prashantaryal07@gmail.com); [kunwarkirtan36@gmail.com](mailto:kunwarkirtan36@gmail.com);  
[navinkhanal3@gmail.com](mailto:navinkhanal3@gmail.com); [dinesh@ioe.edu.np](mailto:dinesh@ioe.edu.np);

<sup>†</sup>These authors contributed equally to this work.

## Abstract

We investigate the use of wavelet-space feature decomposition in neural super-resolution for rendering pipelines. Building on the DFASR framework, we introduce a wavelet-domain representation that separates low- and high-frequency details before reconstruction, enabling the network to better preserve fine textures while maintaining structural consistency. Unlike RGB-space regression, our approach leverages the stationary wavelet transform (SWT) to avoid spatial down-sampling, ensuring alignment across subbands and preserving shift invariance. The model predicts wavelet coefficients conditioned on spatial G-buffers and temporally warped history frames, which are then recombined through inverse wavelet synthesis. We conduct a comprehensive ablation study across wavelet families, transform types, and architectural variants, showing that incorporating SWT improves PSNR by up to 1.5 dB and reduces LPIPS by 17% on average, at a computational overhead of roughly +24 ms compared to our DFASR baseline. While absolute runtimes on our RTX 3050 mobile GPU are higher (141ms) than the original DFASR report on RTX 4090 (11ms), the relative overhead remains modest, suggesting that on higher-end GPUs our method would also remain real-time capable. Taken together, our results suggest that wavelet-domain representations are a principled and effective way to enhance perceptual quality in neural upscaling for graphics applications.

**Keywords:** Real-Time Rendering, Super-Resolution, Wavelet transform

## 1 Introduction

The demand for high-resolution graphics at interactive frame rates has pushed modern rendering pipelines to their computational limits. Physically based shading and real-time ray tracing improve visual fidelity but are often too expensive to run at native resolutions. Neural super-resolution has thus emerged as a practical alternative: frames

are rendered at lower resolution and then reconstructed to the display resolution by learned models, balancing quality and efficiency.

Recent approaches such as NSRR [5], FuseSR [9], and DFASR [7] combine low-resolution renderings with auxiliary scene information like G-buffers and motion vectors. DFASR in particular have demonstrated strong results in arbitrary scale neural super-resolution using Fourier-based INRs. In this work, we revisit this architecture

and investigate whether wavelet-domain representations can further improve reconstruction quality.

We propose a wavelet-domain formulation for neural super-resolution for real-time rendering pipeline. Instead of predicting pixel intensities, our model regresses wavelet coefficients that encode localized frequency information. This explicit spectral representation improves high-frequency reconstruction and reduces blur in textured regions. To avoid resolution loss across subbands, we adopt the stationary wavelet transform (SWT), with inverse reconstruction embedded in the network to allow end-to-end training. Our system supports arbitrary upscaling factors, similar to DFASR, but achieves sharper detail by operating in coefficient space. The approach provides an efficient path toward higher-fidelity rendering within real-time constraints.

## 2 Related Work

This section surveys prior work most relevant to our setting. We begin with neural super-resolution for real-time rendering, focusing on methods that leverage engine metadata, high-resolution G-buffers, and coordinate-based predictors. We then review wavelet-based super-resolution, contrasting discrete and stationary transforms and common strategies that supervise in coefficient and image space. Finally, we summarize BRDF demodulation and evaluation protocols, including perceptual metrics, which frame our experimental design and analysis.

### 2.1 Super-Resolution for Realtime-Rendering

Early neural approaches to real-time upsampling leveraged *engine metadata* (depth, motion vectors) with temporally-aware networks to reconstruct high-resolution frames from low-resolution inputs. Neural Supersampling (NSRR) exemplifies this, formulating reconstruction as a temporally conditioned enhancement task and achieving stable 4× upsampling using dense motion and depth cues [5]. While temporally coherent, these methods remain limited by the LR input, struggling to recover high-frequency detail and typically operate at fixed scale factors [5].

Later work incorporates *high-resolution G-buffers* to provide geometric and material detail

cheaply. FuseSR illustrates this trend, using a multi-resolution fusion architecture (“H-Net”) to align and fuse LR color with HR G-buffers, enabling temporally consistent 4× and 8× upsampling at 4K [9]. This mitigates LR information limits but still depends on discrete scales and accurate multi-resolution alignment.

DFASR advances arbitrary-scale reconstruction with a Fourier-mapped implicit representation, predicting pixel values at requested coordinates while using auxiliary modules for detail and robustness [7]. This removes fixed-scale constraints but introduces sensitivity to Fourier parameterization and frequency-band trade-offs [7]. Complementary methods like ExtraNet focus on *temporal* supersampling, extrapolating future frames with HR G-buffers and motion cues to reduce latency without look-ahead [2].

### 2.2 Wavelets for Super-Resolution

Wavelet-based super-resolution operates in a multi-band frequency domain, separating coarse structure from directional details. Early CNNs like Deep Wavelet Prediction regress subband coefficients and invert the transform, improving high-frequency recovery over direct RGB regression [3]. Later variants integrate convolutional backbones with wavelet analysis/synthesis blocks, achieving consistent gains across SR benchmarks [6].

Two common transforms are the discrete wavelet transform (DWT) and the stationary wavelet transform (SWT). DWT is computationally lighter but shift-variant due to downsampling, which can make learning sensitive to pixel shifts. SWT, in contrast, removes downsampling, producing shift-invariant, full-resolution subbands that preserve fine details across spatial locations, at the cost of higher memory and compute [1]. Most works use single-level decomposition and supervise both coefficient and image space to stabilize training and retain high-frequency fidelity [3, 6]. Common orthogonal families (Haar/db1, Daubechies) are often employed, and the transform choice is typically treated as a modular trade-off between reconstruction quality and runtime efficiency.

### 2.3 BRDFs and Evaluation Metrics

Radiance demodulation separates smooth lighting from high-resolution material detail, applying SR

on lighting and re-modulating with HR materials for sharp textures and temporal stability [4]. Relatedly, pre-integrated BRDFs stabilize filtering/reconstruction [10], and FuseSR shows combining LR color with HR G-buffers plus BRDF demodulation improves  $4\times-8\times$  upsampling [9]. DFASR targets arbitrary-scale reconstruction via Fourier-based implicit representation and spatial-temporal masks rather than BRDF factorization [7].

Evaluation commonly uses PSNR/SSIM, with LPIPS increasingly adopted to better reflect perceptual quality [8]. HDR metrics exist but are less standardized in real-time SR, so many works report tone-mapped results for comparability.

### 3 Method

Our framework extends recent real-time neural super-resolution models by shifting the prediction domain from RGB pixels to wavelet coefficients. While our architecture follows the general coordinate-based design of DFASR [7], our key distinction lies in formulating super-resolution as a wavelet reconstruction task. By predicting frequency-aware subbands and reconstructing through the stationary wavelet transform (SWT), we preserve spatial resolution across coefficients and improve recovery of fine detail. The following subsections introduce the problem setup, data preprocessing pipeline, and network architecture, culminating in our integration of wavelet-domain reconstruction.

#### 3.1 Overview

Our method formulates real-time super-resolution as a wavelet-domain reconstruction problem. The goal is to recover a high-resolution frame  $\hat{I}_{HR}$  from a combination of low-resolution shading, multi-resolution G-buffers, and temporal history. We denote the overall process as

$$\hat{I}_t^{HR} = \text{SR}(I_t^{LR}, G_t^{LR}, G_t^{HR}, I_{t-1}^{HR}, G_{t-1}^{HR}, MV_t, F),$$

where  $I_t^{LR}$  is the current low-resolution frame,  $G_t^{LR}$  and  $G_t^{HR}$  are the low- and high-resolution G-buffers,  $I_{t-1}^{HR}$  is the previous high-resolution frame,  $G_{t-1}^{HR}$  its corresponding G-buffers,  $MV_t$  the motion vectors, and  $F$  the material reflectance information. This compact formulation captures

the pipeline-level data flow, while the details of each component are discussed in later subsections.

Unlike prior approaches that directly regress RGB values, our network predicts a wavelet representation of the target frame. Specifically, it estimates subband coefficients  $\hat{W} = \{\hat{C}_{LL}, \hat{C}_{LH}, \hat{C}_{HL}, \hat{C}_{HH}\}$ , which are subsequently combined through an inverse stationary wavelet transform:

$$\hat{I}_t^{HR} = \mathcal{W}^{-1}(\hat{W}).$$

This shift to the frequency domain enables explicit modeling of high-frequency content while preserving spatial alignment across coefficients. The result is a temporally stable reconstruction with improved detail recovery, particularly at larger upscaling factors.

#### 3.2 Wavelet-Space Formulation

We cast super resolution as prediction in the wavelet domain rather than RGB space. Let  $\mathcal{W}_{\tau,b}$  denote a single-level 2D wavelet analysis operator with transform type  $\tau \in \{\text{DWT}, \text{SWT}\}$  and orthogonal basis  $b$  (for example, Haar, DB4, Sym4). For a target high-resolution image  $I_t^{HR} \in \mathbb{R}^{(sH) \times (sW) \times 3}$ , the corresponding subbands are

$$W_t \triangleq \{C_{LL}, C_{LH}, C_{HL}, C_{HH}\} = \mathcal{W}_{\tau,b}(I_t^{HR}),$$

where  $s$  is the requested scale factor. The network predicts  $\hat{W}_t = \{\hat{C}_{LL}, \hat{C}_{LH}, \hat{C}_{HL}, \hat{C}_{HH}\}$  directly, and the output image is obtained by inverse synthesis,

$$\hat{I}_t^{HR} = \mathcal{W}_{\tau,b}^{-1}(\hat{W}_t).$$

We use a single level of decomposition, which balances frequency separation against runtime. Each color channel is decomposed into four subbands, hence twelve coefficient maps in total. For SWT, subbands preserve spatial size, that is  $C_* \in \mathbb{R}^{(sH) \times (sW) \times 3}$ , which simplifies alignment across branches and avoids resolution loss inside the network. For DWT, subbands are decimated, so we store them in a space-to-depth layout that is convolution friendly and later recover spatial layout with a pixel shuffle prior to inverse synthesis. The inverse wavelet transform is implemented inside the computational graph so gradients flow through  $\mathcal{W}_{\tau,b}^{-1}$  during training.

We primarily use SWT for its shift invariance and resolution preservation, at a modest compute



**Fig. 1:** Single-level wavelet decomposition of an RGB image into  $LL$ ,  $LH$ ,  $HL$ , and  $HH$  subbands per channel. Our network predicts these subbands directly, then applies  $\mathcal{W}_{\tau,b}^{-1}$  to reconstruct  $\hat{I}_t^{HR}$ .

cost due to non-decimated filtering. SWT also requires careful boundary handling. To suppress minor edge artifacts from the learned filters and padded convolutions, we crop a one-pixel border when computing losses during training for SWT configurations. The basis  $b$  is a runtime choice, for example Haar, DB4, or Sym4, and Section 4.4 reports the effect of  $\tau$  and  $b$  on accuracy.

### 3.3 Data Preprocessing and Input Construction

Our model operates in irradiance space, where the shaded image is factorized into BRDF and irradiance components. A low-resolution frame  $I_t^{LR}$  is demodulated using its per-pixel BRDF term  $F_t^{LR}$ :

$$L_t^{LR} = \frac{I_t^{LR}}{F_t^{LR}},$$

where  $L_t^{LR}$  denotes the demodulated irradiance. The network then predicts the high-resolution irradiance  $\hat{L}_t^{HR}$ :

$$\hat{L}_t^{HR} = \mathcal{M}(L_t^{LR}, G_t^{HR}, \text{Warp}(L_{t-1}^{HR}), \Phi),$$

with  $\mathcal{M}$  denoting our wavelet-based reconstruction model. Here  $G_t^{HR}$  is the high-resolution G-buffers,  $\text{Warp}(\cdot)$  is temporal reprojection of the previous irradiance frame using motion vectors  $MV_t$ , and  $\Phi = \{\Phi_{\text{spat}}, \Phi_{\text{temp}}\}$  are spatial and temporal masks as introduced in [7].

The G-buffers contain albedo ( $A$ ), normals ( $N$ ), depth ( $D$ ), roughness ( $R$ ), and metallic ( $M$ ), from which per-pixel BRDF factors ( $F =$



Rendered Frame      BRDF      Irradiance

**Fig. 2:** Illustration of BRDF demodulation. The left shows the rendered frame, the middle the BRDF term and the right the demodulated irradiance. This decomposition highlights how BRDF demodulation extracts away the high frequency textures so that model can focus on low frequency lighting component only.

$\{F_t^{LR}, F_t^{HR}, F_{t-1}^{HR}\}$ ) are derived. After super-resolution, the final shaded output is obtained by remodulation:

$$\hat{I}_t^{HR} = F_t \cdot \hat{L}_t^{HR},$$

which restores view- and lighting-dependent effects. This formulation shifts the network’s focus toward reconstructing frequency content in irradiance space, while high-resolution geometric cues from  $G_t$  ensure accurate remodulation in the final image.

### 3.4 Network Architecture

Our model adapts the DFASR backbone but shifts the output space to wavelet coefficients. As shown in Fig. 3, the network processes inputs through dedicated feature extractors, and combines them via a feature fusion path and a Fourier-mapped INR branch. The combined output is reconstructed into the final image using the inverse wavelet transform.

#### 3.4.1 Feature Extractors

Our model employs three dedicated feature extractors tailored to the input modalities: a low-resolution frame extractor (LR-FE), a high-resolution G-buffer extractor (GB-FE), and a temporal extractor (T-FE). Each produces a compact representation aligned to the target resolution and contributes complementary cues for wavelet prediction.

The **LR-FE** processes the pixel-unshuffled, demodulated low-resolution input frame  $I_t^{LR}$ ,

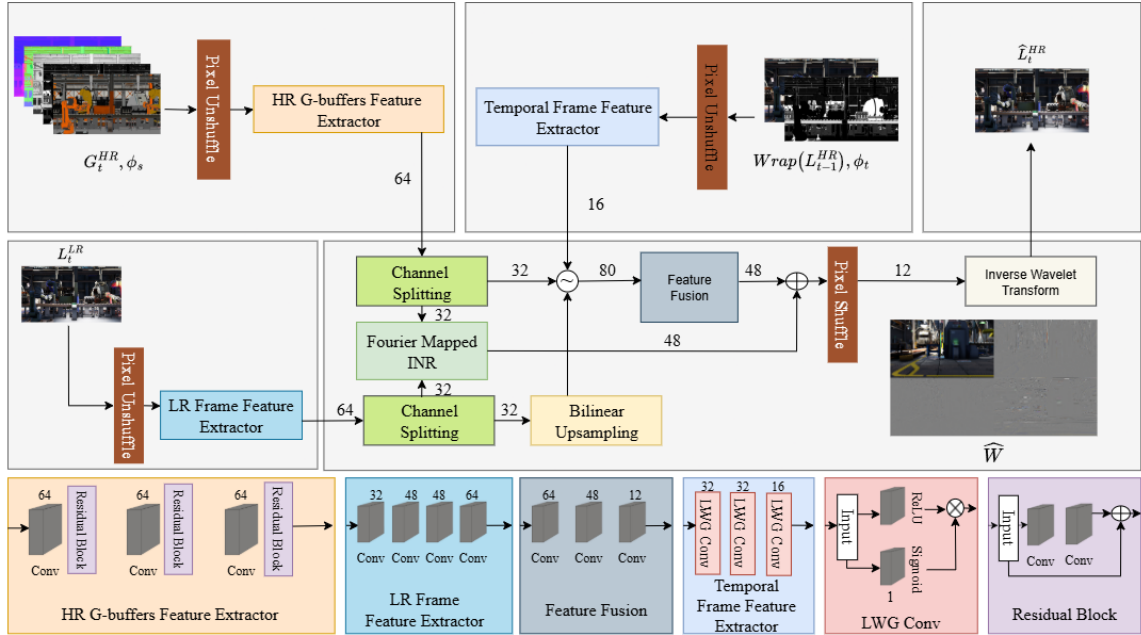


**Fig. 3:** Overview of our network architecture. The model consists of three feature extractors (for LR frames, HR G-buffers, and temporal inputs), a convolutional fusion branch, and an implicit neural representation (INR) branch with Fourier feature mapping. Their outputs are combined in the wavelet domain and reconstructed into the final image via inverse wavelet transform and pixel shuffle.

using a stack of  $3 \times 3$  convolutions to produce a feature map later routed to both fusion and INR pathways. The **GB-FE** encodes the high-resolution G-buffers  $G_t^{HR}$  through residual blocks, extracting geometry- and material-aware information such as depth and surface orientation at display resolution. The **T-FE** receives the warped previous frame  $\text{Warp}(I_{t-1}^{HR}, MV_t)$  together with temporal masks, and is implemented with lightweight gated convolutions (LWGC) to balance motion sensitivity and efficiency.

Together, these extractors provide complementary signals: LR features represent coarse appearance, HR G-buffers supply high-frequency geometric guidance, and temporal features capture frame-to-frame coherence. Their outputs serve as the basis for subsequent fusion and wavelet-domain reconstruction.

### 3.4.2 Feature Fusion

The feature fusion module aggregates information from three complementary sources: low-resolution frame features, high-resolution G-buffer features,

and temporally aligned features from the previous frame. This combined representation captures both spatial and geometric context, providing the structural backbone of the reconstruction. The fusion branch is responsible for generating the coarse wavelet-domain prediction, while the implicit neural representation (INR) branch contributes finer local corrections. Their outputs are combined element-wise to form the final set of predicted wavelet coefficients, which are later synthesized into the high-resolution image.

### 3.4.3 Implicit Neural Representation (INR)

To support arbitrary-scale super-resolution while enhancing localized high-frequency detail, we employ a coordinate-based Implicit Neural Representation (INR) branch. Prior works such as DFASR [7] demonstrated the effectiveness of Fourier-mapped INRs for rendering-aware upscaling. Building on this idea, we adapt the design to predict wavelet-domain features rather than RGB pixels, which provides finer frequency separation and improved detail recovery.

For each HR pixel coordinate  $x$ , we compute a Fourier embedding

$$\mathcal{F}(x) = A(x) \cdot \begin{bmatrix} \cos(\pi\langle F(x), x \rangle + \phi(x)) \\ \sin(\pi\langle F(x), x \rangle + \phi(x)) \end{bmatrix},$$

where  $A(x)$  is an amplitude term derived from LR features,  $F(x)$  is a frequency term guided by HR G-buffer features, and  $\phi(x)$  is a spatial phase offset. These embeddings are passed through a lightweight multi-layer perceptron (MLP), producing predictions in wavelet space.

The INR complements the fusion module by injecting coordinate-aware, high-frequency corrections. Their outputs are combined element-wise to form the final set of predicted coefficients. Together, the two branches balance structural fidelity with detail sharpness, while the continuous INR mapping enables reconstructions at arbitrary scale factors.

### 3.4.4 Reconstruction

The final reconstruction stage aggregates the outputs from the feature fusion and INR branches, which are element-wise combined to form the estimated wavelet coefficients. These coefficients are subsequently passed through a reconstruction layer consisting of a lightweight convolution and a single-level inverse wavelet transform (IWT), following the formulation already introduced in Sec. 3.2. This yields the super-resolved output image.

Our implementation supports configurable reconstruction settings: the wavelet basis can be selected at runtime (e.g., Haar, Daubechies), and both discrete (DWT) and stationary (SWT) variants are available. By default, the reconstruction is performed with a single-level discrete transform, but the flexibility of our framework allows controlled experimentation with different bases and transform types.

The resulting output is produced in HDR linear space. For visualization purposes, we apply tonemapping during evaluation, but training and inference operate directly in the HDR domain to preserve photometric consistency.

### 3.4.5 Loss Functions

Training is guided by a composite objective that balances fidelity in both the image and wavelet

domains. We combine (i) an  $\ell_1$  loss on predicted wavelet coefficients, (ii) an  $\ell_1$  reconstruction loss in image space, (iii) perceptual similarity terms using SSIM and LPIPS, and (iv) spatial mask and temporal consistency losses following DFASR [7]. The total loss is

$$\begin{aligned} \mathcal{L}_{total} = & \lambda_w \mathcal{L}_{waveletL1} + \lambda_i \mathcal{L}_{imageL1} + \lambda_s \mathcal{L}_{SSIM} \\ & + \lambda_p \mathcal{L}_{LPIPS} + \lambda_m \mathcal{L}_{mask} + \lambda_t \mathcal{L}_{temporal} \end{aligned}$$

This formulation enforces accuracy across spectral, perceptual, and temporal dimensions, ensuring stable reconstructions under real-time rendering.

## 4 Results

### 4.1 Evaluation Setup

We evaluate our method on a custom Unreal Engine 4.27 dataset containing diverse indoor and outdoor scenes, including urban environments, industrial interiors, and stylized game assets. The dataset comprises approximately 3700 training frames, 700 validation frames, and 1000 test frames, drawn from seven distinct scenes, details in Table 1. High-resolution (HR) frames are rendered at  $1920 \times 1080$  resolution along with their corresponding high-resolution G-buffers. To generate low-resolution (LR) inputs, we apply nearest-neighbor downsampling at random scales between  $2.0 \times$  and  $4.0 \times$  during training, enabling arbitrary-scale inference. Dataset extraction was facilitated by a custom Unreal Engine plugin, adapted from the Extranets engine modification [2], allowing automated capture of both shading outputs and auxiliary buffers.

### 4.2 Quantitative Comparison

We compare our proposed wavelet-space super-resolution framework against the ‘‘No Wavelet’’ variant (equivalent to DFASR’s architecture but trained on our dataset) and other ablation configurations. The main evaluation is performed at  $\times 2$  upscaling, which is representative of the quality trends across other scales. We report PSNR, SSIM, and LPIPS on the held-out test scenes. For a fair comparison, we also evaluate the publicly available DFASR model on three scenes that are not part of its training set: *Eastern Village*,

**Table 1:** Dataset composition with train/validation/test split for each scene. All frames are rendered at  $1920 \times 1080$  with HR G-buffers and downsampled for LR inputs.

| Scene             | Train | Val | Test |
|-------------------|-------|-----|------|
| Eastern Village   | 555   | 100 | 285  |
| Abandoned Factory | 740   | 100 | 0    |
| Brass City        | 740   | 100 | 0    |
| City Park         | 740   | 100 | 0    |
| Factory Interior  | 555   | 100 | 185  |
| Slay              | 370   | 100 | 185  |
| Downtown Alley    | 0     | 100 | 185  |
| Downtown West     | 0     | 0   | 285  |
| <b>Total</b>      | 3700  | 700 | 1000 |

*Downtown Alley*, and *Downtown West*, given in Table 3.

Table 2 shows the results, with the best values highlighted in bold. Our best-performing configuration, **SWT with DB4 wavelet**, achieves the highest PSNR and SSIM, and the lowest LPIPS across most scenes. Compared to the “No Wavelet” baseline, it improves PSNR by **1.5 dB** and reduces LPIPS by **0.022** on average, maintaining stable performance across all content types. Although SWT DB4 yields the best quality, it also incurs a higher inference time, which is discussed in Section 4.5.

We report Peak Signal-to-Noise Ratio (PSNR), Structural Similarity Index (SSIM), and Learned Perceptual Image Patch Similarity (LPIPS) [8]. PSNR and SSIM are computed in the normalized HDR space using gamma correction and value clipping, while LPIPS uses the AlexNet backbone during training and the VGG backbone for final evaluation. For each test scene, we compute metrics for upsampling factors of  $2\times$ ,  $3\times$ , and  $4\times$ , and report their averages.

All models are trained end-to-end using a patch size of  $432 \times 432$  and a batch size of 8. Evaluation is performed on full-resolution frames without cropping.

### 4.3 Qualitative Comparison

While quantitative metrics such as PSNR, SSIM, and LPIPS provide useful averages, they do not

**Table 2:** Quantitative comparison of methods ( $3\times$  upscaling). Best results in bold.

| Method     | PSNR $\uparrow$ | LPIPS $\downarrow$ | SSIM $\uparrow$ |
|------------|-----------------|--------------------|-----------------|
| No Wavelet | 28.9            | 0.136              | 0.897           |
| DWT Haar   | 29.4            | 0.124              | 0.905           |
| SWT Haar   | 29.7            | 0.117              | 0.912           |
| SWT DB4    | <b>30.4</b>     | <b>0.114</b>       | <b>0.920</b>    |

always capture perceptual differences. We therefore present visual comparisons against key baselines, focusing on regions with fine textures, sharp edges, and high-frequency structures.

Across representative examples at  $2\times$  (and one case at  $3\times$ ) upscaling, the no-wavelet baseline (NoWave) preserves overall structure but often smooths out high-frequency detail. DFASR improves sharpness but can still exhibit ringing artifacts or residual blur in challenging regions. Our SWT-based model shows modest improvements in edge clarity and texture fidelity, particularly in repeated patterns, foliage, and diagonal structures. As shown in Figure 6, SWT restores edges slightly more faithfully than both DFASR and NoWave, reflecting the benefit of processing in wavelet space. In the first and second scenes, the model demonstrates improved color fidelity and edge preservation, while in the final scene it exhibits reduced color errors, resulting in more visually consistent reconstruction.

These visual observations align with the quantitative trends, indicating that the wavelet-space formulation provides a small but consistent improvement in high-frequency detail reconstruction.

### 4.4 Ablation Study

To better understand the contributions of different design choices, we group ablations into two categories: *wavelet formulation* and *architectural/training variants*. All results are reported at  $2\times$  upscaling on tone-mapped outputs.

#### *Wavelet formulation.*

We compare discrete wavelet transform (DWT) against stationary wavelet transform (SWT), and evaluate different wavelet bases. This isolates the

**Table 3:** Quantitative comparison with DFASR across scenes ( $3\times$  upscaling). Best results in bold.

| Method         | Eastern Village |                    |                 | Downtown Alley  |                    |                 | Downtown West   |                    |                 |
|----------------|-----------------|--------------------|-----------------|-----------------|--------------------|-----------------|-----------------|--------------------|-----------------|
|                | PSNR $\uparrow$ | LPIPS $\downarrow$ | SSIM $\uparrow$ | PSNR $\uparrow$ | LPIPS $\downarrow$ | SSIM $\uparrow$ | PSNR $\uparrow$ | LPIPS $\downarrow$ | SSIM $\uparrow$ |
| SWT DB4 (Ours) | <b>29.7</b>     | <b>0.115</b>       | <b>0.888</b>    | <b>36.8</b>     | <b>0.059</b>       | <b>0.960</b>    | <b>28.5</b>     | <b>0.144</b>       | <b>0.872</b>    |
| DFASR          | 28.2            | 0.180              | 0.850           | 32.5            | 0.152              | 0.903           | 26.7            | 0.250              | 0.763           |

effect of transform type and basis on reconstruction quality.

#### Architectural and training variants.

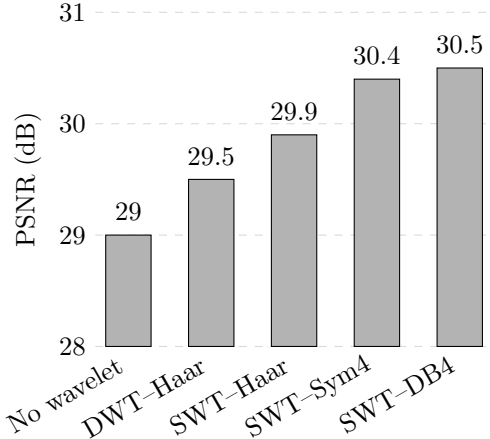
We further investigate alternative network designs: (1) **Fusion $\rightarrow$ LL, INR $\rightarrow$ others (SWT-Haar)** restricts the fusion path to predict the low-frequency LL subband, while the INR predicts the high-frequency subbands (LH, HL, HH). (2) **Multi-INR (DWT-Haar)** assigns a separate INR branch to each subband instead of a shared INR, testing whether coefficient-wise specialization improves results. (3) **Single-scale ( $2\times$  only, DWT-Haar)** trains the model exclusively on  $2\times$  upscaling instead of arbitrary-scale sampling, measuring whether multi-scale training compromises single-scale fidelity.

**Table 4:** Wavelet formulation ablation at  $2\times$  upscaling. Metrics are computed on tone-mapped outputs. Best results are highlighted in bold.

| Configuration         | PSNR $\uparrow$ | LPIPS $\downarrow$ | SSIM $\uparrow$ |
|-----------------------|-----------------|--------------------|-----------------|
| No wavelet (baseline) | 29.0            | 0.135              | 0.899           |
| DWT-Haar              | 29.5            | 0.122              | 0.906           |
| SWT-Haar              | 29.9            | 0.114              | 0.913           |
| SWT-Sym4              | 30.4            | 0.116              | 0.921           |
| SWT-DB4               | <b>30.5</b>     | <b>0.112</b>       | <b>0.922</b>    |

#### Takeaways.

Overall, the ablation results show that SWT consistently outperforms DWT, with the DB4 basis giving the highest reconstruction quality among all tested configurations. Alternative architectural variants such as Fusion-LL and Multi-INR reduce performance, indicating that a unified INR

**Fig. 4:** PSNR comparison of ablation configurations at  $2\times$  upscaling. Values correspond to Table 4. We plot PSNR only for clarity, as SSIM and LPIPS follow the same trend.**Table 5:** Architectural and training ablations at  $2\times$  upscaling. Each variant is evaluated with its native wavelet transform.

| Configuration           | PSNR $\uparrow$ | LPIPS $\downarrow$ | SSIM $\uparrow$ |
|-------------------------|-----------------|--------------------|-----------------|
| SWT-Haar                | 29.9            | 0.114              | 0.913           |
| Fusion-LL (SWT-Haar)    | 29.7            | 0.120              | 0.910           |
| DWT-Haar                | 29.5            | 0.122              | 0.906           |
| Multi-INR (DWT-Haar)    | 29.4            | 0.126              | 0.905           |
| Single-scale (DWT-Haar) | 29.7            | 0.123              | 0.909           |

with joint coefficient prediction is more effective. Finally, multi-scale training improves generalization without sacrificing fixed-scale accuracy, demonstrating the robustness of our chosen setup.

## 4.5 Runtime and Efficiency

We evaluate inference performance at  $2\times$  upscaling for  $1920 \times 1080$  output on an RTX 3050

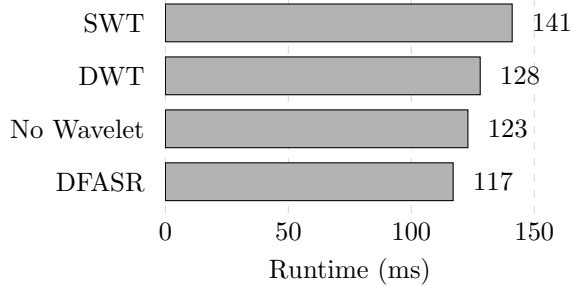


**Fig. 5:** Average runtime per frame at  $2\times$  upscaling,  $1920 \times 1080$  output resolution, measured on RTX 3050 mobile.

mobile GPU, using single-frame inference without low-level optimizations. Figure 5 reports average per-frame runtimes across methods. Our No-Wavelet baseline is close to DFASR but runs  $\sim 6$  ms slower, which we attribute to hardware and implementation differences (DFASR reports 11 ms on an RTX 4090). Introducing wavelet transforms increases runtime: DWT variants add  $\sim 5$  ms overhead relative to the No Wavelet baseline, while SWT adds  $\sim 18$  ms. This reflects a clear accuracy–efficiency trade-off: SWT with DB4 provides the best perceptual quality but incurs additional runtime cost.

Absolute runtimes on the RTX 3050 mobile are higher ( $\sim 141$  ms) than DFASR’s published results on the RTX 4090 (11 ms), due to the lack of RT cores and FP16 acceleration. However, since our relative overhead compared to the DFASR baseline is modest (+24 ms), we expect that on high-end GPUs our approach would also remain real-time capable, consistent with DFASR’s original claims.

## 5 Conclusion

We have presented a wavelet-domain super-resolution framework for real-time rendering pipelines that predicts frequency-aware subbands rather than directly regressing RGB values. By combining convolutional feature extractors, an implicit neural representation branch with Fourier mapping, and stationary wavelet reconstruction, our method achieves detail-preserving and resolution-consistent upscaling across arbitrary scale factors. This formulation leverages the

efficiency of G-buffer inputs and BRDF demodulation to recover fine shading and geometric details at reduced rendering cost. Experimental results demonstrate that the approach effectively captures high-frequency content while maintaining compatibility with standard rendering pipelines.

Despite these advantages, several limitations remain. Temporal consistency is less robust than in specialized video super-resolution methods, and the current system is restricted to a single-level wavelet decomposition. Moreover, while the design supports real-time performance in principle, further optimization is needed for deployment in latency-sensitive applications. These aspects highlight opportunities for extending the method with stronger temporal modeling and more expressive multi-level wavelet representations.

Looking forward, several directions can improve the utility of our framework. Integrating multi-scale wavelet hierarchies could enhance the capture of both global structures and fine textures. More advanced temporal modules may improve stability across frames, particularly in dynamic scenes. Adapting the network for integer-precision inference would bring the design closer to industrial deployment on modern GPUs and consoles, where INT inference is standard. Finally, coupling the method with emerging real-time ray tracing pipelines offers a promising avenue to exploit richer lighting information within the same frequency-aware framework. Together, these extensions open the path toward more practical, robust, and efficient real-time super-resolution systems.

## Acknowledgments

The authors would like to express their sincere gratitude to Er. Saroj Shakya for his invaluable guidance and support as a co-supervisor throughout the duration of this project. We would also like to thank Ashim Tiwari for providing the necessary computational resources, which were essential for the successful completion of our work. Special thanks go to Ashim Bhharai for his practical assistance and hands-on support during the implementation phase of the project.

## References

- [1] Farah Deeba, She Kun, Fayaz Ali Dharejo, and Yuanchun Zhou. Wavelet-based enhanced medical image super resolution. *IEEE Access*, 8:37035–37044, 2020.
- [2] Jie Guo, Xihao Fu, Liqiang Lin, Hengjun Ma, Yanwen Guo, Shiqiu Liu, and Ling-Qi Yan. Extranet: Real-time extrapolated rendering for low-latency temporal super-sampling. *ACM Trans. Graph.*, 40(6), dec 2021.
- [3] Tiantong Guo, Hojjat Seyed Mousavi, Tiep Huu Vu, and Vishal Monga. Deep wavelet prediction for image super-resolution. In *2017 IEEE Conference on Computer Vision and Pattern Recognition Workshops (CVPRW)*, pages 1100–1109, 2017.
- [4] Jia Li, Ziling Chen, Xiaolong Wu, Lu Wang, Beibei Wang, and Lei Zhang. Neural super-resolution for real-time rendering with radiance demodulation, 2024.
- [5] Lei Xiao, Salah Nouri, Matt Chapman, Alexander Fix, Douglas Lanman, and Anton Kaplanyan. Neural supersampling for real-time rendering. *ACM Trans. Graph.*, 39(4), August 2020.
- [6] Hui Yang and Yibo Wang. An effective and comprehensive image super resolution algorithm combined with a novel convolutional neural network and wavelet transform. *IEEE Access*, 9:98790–98799, 2021.
- [7] Haonan Zhang, Jie Guo, Jiawei Zhang, Haoyu Qin, Zesen Feng, Ming Yang, and Yanwen Guo. Deep fourier-based arbitrary-scale super-resolution for real-time rendering. In *ACM SIGGRAPH 2024 Conference Papers*, pages 1–11, 2024.
- [8] Richard Zhang, Phillip Isola, Alexei A. Efros, Eli Shechtman, and Oliver Wang. The unreasonable effectiveness of deep features as a perceptual metric, 2018.
- [9] Zhihua Zhong, Jingsen Zhu, Yuxin Dai, Chuankun Zheng, Guanlin Chen, Yuchi Huo, Hujun Bao, and Rui Wang. Fusesr: Super resolution for real-time rendering through efficient multi-resolution fusion. In *SIGGRAPH Asia 2023 Conference Papers*, pages 1–10, 2023.
- [10] Tao Zhuang, Pengfei Shen, Beibei Wang, and Ligang Liu. Real-time Denoising Using BRDF Pre-integration Factorization. *Computer Graphics Forum*, 2021.

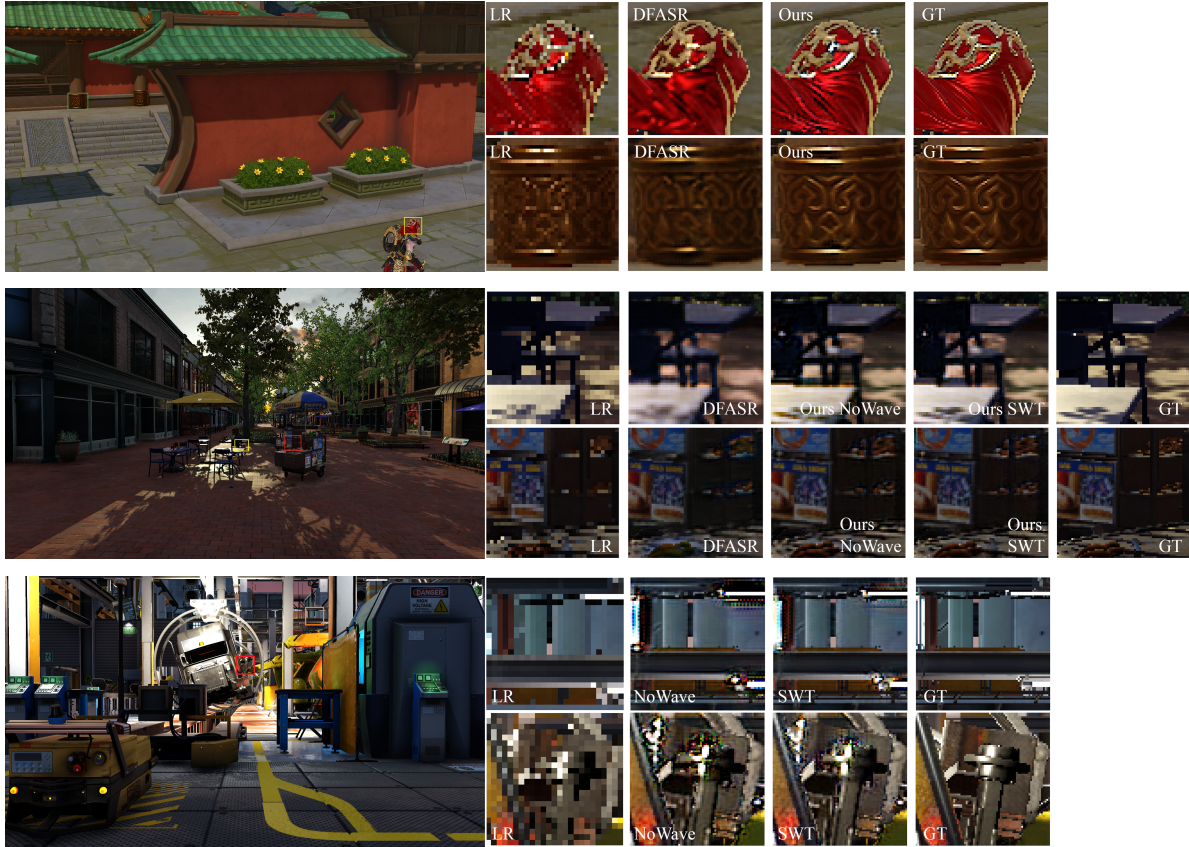


**Fig. 6:** Upscaling results on multiple scenes using NoWave, DFASR [7], and our SWT model. The first and second scenes show  $2\times$  upscaling, while the third scene shows  $3\times$  upscaling. Our SWT model consistently preserves edges and fine details better than the baselines, producing sharper and cleaner outputs across all tested scenarios.